(NAPC-2018-026)

Numerical Investigation of Three-Dimensional Separation in Twisted Turbine Blade: The Influence of Endwall Boundary Layer State

Gaurav Saxena
Department of Mechanical Engineering ,
Indian Institute of Technology Kanpur, Kanpur.
Email: gsaxena@iitk.ac.in

Arun K Saha
Department of Mechanical Engineering ,
Indian Institute of Technology Kanpur, Kanpur.
Email: aksaha@iitk.ac.in

Ritesh Gaur
Scientist E, Gas Turbine Research
Establishment (GTRE),Bangalore
Email: riteshgaur@gtre.drdo.in

ABSTRACT

The substantial adverse pressure gradient experienced by a turbulent boundary layer while approaching an endwall mounted twisted turbine blade and caused the impending flow to separate three-dimensionally to form a dynamically active horseshoe vortex (HSV) system in the junction of the turbine blade with endwall. The large eddy simulations (LES) of the flow past a twisted turbine blade mounted on a curved endwall with periodic boundary condition in pitchwise direction is carried out for Re = 50000 to methodically investigate the HSV dynamics. The significant variations with Re in terms of mean flow quantities, heat transfer distribution & coherent dynamics of turbulent HSV are shown in computed results. The HSV system consists of a multiple number of necklace type vortices that are shed periodically at maximal frequencies. For high Re, we show that outburst of wall govern the instantaneous flow field, averaged vorticity affiliate with the growth of hairpin vortices that enclose around and dislocate the primary HSV. The time-mean endwall heat transfer is prevailed by two bands of high heat transfer which encircle the leading edge of the blade. The band of maximal heat transfer, occurs in the corner region of the juncture while the secondary high heat transfer band (thin as compare to primary) develops upstream of primary band, in between primary & secondary band a relatively low heat transfer region is identified.

NOMENCLATURE

SGS	Subgrid scale structures
HSV	Horseshoe vortex

SISM	Shear Improved Smagorinsky Model
FVM	Finite Volume Method
MIM	Momentum Interpolation Method
FOU	First Order Upwind
QUICK	Quadratic Upwind Interpolation Convective Kinematics
GSOR	Gauss–Seidel over-relaxation
CDS	Central Difference Scheme
Pr_{SGS}	Turbulent Prandtl number

INTRODUCTION

Junction flows may experience from secondary flows such as horseshoe vortices and corner separations that can dramatically diminish the performance of aircraft. The substantial adverse pressure gradient is experienced by a turbulent boundary layer while approaching an endwall seated turbine blade and it goes through a three-dimensional separation forming a horseshoe vortex (HSV) system that muffles around the blade like a string. The existence of the turbine blade influences the mean flow distribution upstream of the juncture. In the juncture, the secondary flow system transports turbulence and mutate the mean flow, thus having a consequential effect on the distribution of turbulent stresses, the separation vortex plays an imperative role in this process. The junction flows in particular turbine blade hub-junctions are relevant to many engineering problems, i.e., lateral wings of the submarine, plate heat exchanger, flow past surface mounted cylinder (circular & rectangular). In the pioneering work, of Devenport & Simpson, [1] investigated in detail the HSV structure at Re = 1.15×10^5 is

formed in the base of leading edge of a cylindrical wing explore the rich dynamics by analyzing their experimental measurement at the plane of symmetry. Their results showed that the HSV is distinguished by coherent low-frequency oscillations that generate the bimodal histogram of streamwise & spanwise velocity probability density function (pdfs) close to the wall at the symmetry plane. Similar typical features in the turbulent stresses and complex interactions of vortical structures have also been measured around other configurations [2, 3, 4, 5]. Simpson, [6] revealed that many factors affect the evolution & dynamics of the HSV system, the presence of wall mounted obstacle in the flow field created the adverse pressure gradient that determined by the geometrical features of the obstruction in the boundary flow. The evolution of complex HSV system is influenced by the flow Reynolds number along with boundary layer thickness that produces the high turbulent stresses at the leading edge of the wall mounted obstacles [6, 7]. Baker, [8] investigated the formation of turbulent HSV in front of a wall mounted cylinder. Oil & smoke flow visualization suggests that only four vortex system exist (i.e. for $4000 < UD/\upsilon < 90000$, $4 < D/\delta* < 30$). He reported [8] that at the location of primary horseshoe vortex pressure distribution pretence least possible magnitude. By measuring the near wall pressure Baker, [8] was first to determine the qualitative influence of the boundary layer on the average position of the primary HSV, observing that the HSV system moves closer to cylinder when $D/\delta*$ increases. Dargahi, [9] studied the flow around a vertical cylinder mounted in a rectangular channel. Hydrogen bubble flow visualization and hot film measurements were carried out for Reynolds number between 6.6×10^3 & 6.5×10^4 they showed the similar flow patterns that are observed in [8]. Instantaneous flow visualization techniques using a laser sheet and time resolved estimation of the wall induced pressure, that are carried out by Agui and Andreopoulos, [10] the results point out that the primary vortex consists of multiple large scale structures which have begun in the impending boundary layer and have drawn substantial additional vorticity, their measurements indicate that the rms pressure fluctuations increases as separation is approached and reach a maximum near attachment. Also reported [10], a highly intermittent quasi periodic flow. In the upstream of cylinder a continuous eruption of near -wall fluid originating between the wall and the main horseshoe vortex, generating mushroom-like vortical structures that were lifted off the wall and interacted with the primary vortex. Many cases of vortex eruptions documented by Doligalski, [7] produced by vortical structures near solid walls and formed the relation between secondary coherent vortices that are generating due to these bursting phenomenon with the ejection of counter clockwise rotating vorticity that engulfed the large structures. He reported [7] that at the symmetry plane in a junction region formed by the obstacle & endwall, the vorticity spikes are noticed that accord to three-dimensional configuration of hairpin vortices that build on top of the primary HSV, these hairpin vortices create the instability among the vortex while generating the eruptions when the merging between the vortical structure begin. Similar observations for laminar junction flows has also been reported [11, 12] in that the emergence of the counter clockwise rotating vorticity spikes from the wall is observed

that interact with HSV system, generating its deterioration and periodic restoration. The computational simulation in case of junction flow is quite challenging, to capture the correct flow physics in the HSV system the selection of accurate numerical scheme is essential at high Reynolds number. The experimental result of Devenport & Simpson, [1] has been widely studied by using the computational method such as steady & unsteady Reynolds-averaged Navier-Stokes (RANS & URANS) turbulence models, including linear & nonlinear eddy viscosity models and second-moment closure models [13, 14, 15]. The following are the significant suggestions from the study of [13, 14, 15, 16] are summarized as follows: The RANS & URANS have naturally failed to capture the unsteadiness of the HSV system as well as unable to predict the exact location and the shape of mean HSV even though the correct prediction of turbulence statistics in the proximity of junction is not well captured. The numerical simulation-establish on second moment closure models have been only able to interpret better result than eddy viscosity model. The size & the core location of the mean horseshoe structure can correctly approximate by second-moment closure models. The turbulence intensities near the endwall & obstacle region are carefully resolved [13, 15, 16] but these more refined RANS models have failed to provide a very accurate prediction of the turbulent kinetic energy (C-shaped, double peak structures), the spatial distribution of the vortical structures or to give any insights on the bimodal dynamics of turbulent fluctuations. Devenport & Simpson, [1] also identifies the limitations of standard RANS methods for this flow and is also discussed in the recent review by Simpson, [6]. Large eddy simulation (LES) is the better option for simulating mutinous flows with reasonable computational resources. In LES all the scales except the energy dissipating Kolmogorov scales are resolved. LES entirely resolves all the unsteady motion from substantial energy containing scales to the inertial range, it can be expected to be more accurate and reliable then RANS. LES is able to capture all the correct physics associated with the dynamics of HSV system. The several such studies have been reported in the literature [16-19]. For surface mounted cube at Re = 40000, many LES computations have been performed their result reveal that calculated flow in the HSV region exhibit bimodal oscillations thus confirming the experimental findings [16-20]. The critical observation from LES simulations is that the stipulation of time-dependent, turbulent like inflow boundary condition is an essential for correctly predicting the location of HSV reported through experimentally, the steady inflow conditions when using with the LES simulations that are proficient in capturing the instability in the junction regions but the figured HSV is moderately upstream from its actual position [18, 19]. The instantaneous & time averaged flow topology and the associated heat transfer in the leading edge endwall region of a symmetric airfoil are discussed by Praisner et al., [33, 34] the heat transfer is dominated by two bands of high heat transfer, which circumscribe the leading edge of the obstacle. The band of highest heat transfer occurs in the corner region of the juncture, reflecting a 350 % increase over the impinging turbulent boundary layer. The secondary high heat transfer band develops upstream of the primary band, reflecting a 250 % heat transfer

2

increase and is characterized by high level of fluctuating heat load.

NUMERICAL METHODOLOGY

1. Governing equations & LES model

In the present study, Newtonian, unsteady, incompressible Navier-Stokes equation along with energy equations in primitive variable form are employed to simulate the fluid flow and heat transfer through twisted turbine blade passage. The governing equations for LES are obtained by applying spatial filter (top-hat), to the Navier-Stokes and the energy equations to explicitly separate the large and subgrid scale structures (SGS), the equation in dimensionless form Saha & Acharya, [21] are expressed as

$$\frac{\partial \bar{u}_i}{\partial x_i} = 0 \tag{1}$$

$$\frac{\partial \bar{u}_i}{\partial t} + \frac{\partial \bar{u}_i \bar{u}_j}{\partial x_j} = -\frac{\partial \bar{p}}{\partial x_i} + \frac{1}{\mathrm{Re}} \frac{\partial^2 \bar{u}_i}{\partial x_j^2} + \frac{\partial \tau_{ij}}{\partial x_j} \tag{2}$$

$$\frac{\partial \bar{\theta}}{\partial t} + \frac{\partial \bar{u}_j \bar{\theta}}{\partial x_j} = \frac{1}{\mathrm{Re}\,\mathrm{Pr}} \frac{\partial^2 \bar{\theta}}{\partial x_j^2} + \frac{\partial q_j}{\partial x_j} \tag{3}$$

$$\tau_{ij} = \overline{u_i u_j} - \bar{u}_i \bar{u}_j = \overline{u_i' u_j'}$$
$$q_j = -\overline{u_j' \theta'} \tag{4}$$

Where τ_{ij} & q_{ij} is the SGS stress tensor & subgrid scale energy flux. The governing equations are non-dimensionalized using length scale C i.e. the axial chord of blade, velocity scale as u_{avg}, pressure by ρu_{avg}^2 and time with C/u_{avg}. The Reynolds number (Re) is hence defined as $\mathrm{Re} = u_{avg} C / \nu$. Temperature is non-dimensionalized using a scale $\theta = (T - T_w)/(T_{m1}(t) - T_w)$, where T_w is the wall temperature and $T_{m1}(t)$ is the bulk temperature of the fluid evaluated at inlet of the computational domain. The SGS models as based on the gradient transport hypothesis correlating τ_{ij} to the large scale strain-rate tensor (equation (5)) while the strain rate is $\bar{S}_{ij}$ shown in equation (6)

$$\tau_{ij} = -2\nu_T \bar{S}_{ij} + \frac{1}{3}\delta_{ij}\tau_{kk} \quad \& \quad \tau_{kk} = \overline{u_k' u_k'} \tag{5}$$

$$\bar{S}_{ij} = \frac{1}{2}\left\{ \frac{\partial \bar{u}_i}{\partial x_j} + \frac{\partial \bar{u}_j}{\partial x_i} \right\} \tag{6}$$

On substituting, equations (4) & (5) in (2) the final form of the filtered Navier-Stokes equation can be written as

$$\frac{\partial \bar{u}_i}{\partial t} + \frac{\partial \bar{u}_i \bar{u}_j}{\partial x_j} = -\frac{\partial \bar{p}}{\partial x_i} + \frac{\partial}{\partial x_j}\left[\left(\frac{1}{\mathrm{Re}} + \nu_T \right) \frac{\partial \bar{u}_i}{\partial x_j} \right] + \frac{\partial}{\partial x_j}\left(\nu_T \frac{\partial \bar{u}_j}{\partial x_i} \right) \tag{7}$$

The subgrid scale energy flux, $q_j = -\overline{u_j' \theta'}$ in the Equation (4) is given by Murata et al., [22] as shown in Equation (8). Substitute equation (8) in (3), the final form of energy equation is given by Equation (9)

$$q_j = \frac{\nu_T}{\mathrm{Pr}_{SGS}} \frac{\partial \bar{\theta}}{\partial x_j} \tag{8}$$

$$\frac{\partial \bar{\theta}}{\partial t} + \frac{\partial \bar{u}_j \bar{\theta}}{\partial x_j} = \left(\frac{1}{\mathrm{Re}\,\mathrm{Pr}} + \frac{\nu_T}{\mathrm{Pr}_{SGS}} \right) \frac{\partial^2 \bar{\theta}}{\partial x_j^2} \tag{9}$$

In equation (9) Pr_{SGS} is the turbulent Prandtl number for subgrid-scale components and in the present study its value is kept fixed to 0.5 as suggested in Moin et al., [23]. Smagorinsky, [24] proposed model in which the eddy viscosity defined by equation $\nu_T = (C_S \bar{\Delta})^2 |\bar{S}|$, in which C_S is called the Smagorinsky constant whose value lies in the range 0.065-0.25 and $|\bar{S}| = (2S_{ij}S_{ij})^{1/2}$, where S_{ij} is the strain rate. There are certain drawbacks of Smagorinsky model (i) it is highly dissipative (ii) it cannot account for backscatter of energy from smaller to larger structure as the turbulent viscosity is always positive. So the model is unable to capture the true transition to turbulence to overcome this problem Lévêque, [25] modified the Smagorinsky model & defined eddy viscosity as $\nu_T = (C_S \bar{\Delta})^2 \left(|\bar{S}| - |\langle \bar{S} \rangle| \right)$, where $|\langle \bar{S} \rangle|$ is the mean shear & whereas $|\bar{S}|$ is the instantaneous resolved rate of strain tensor while doing the ensemble averaging the mean shear rate is obtained which can be averaged spatially over the homogenous direction or an average in temporal direction. This proposed model is called as Shear Improved Smagorinsky model (SISM). In proposed model, the effect of mean gradient is removed venerating the energy budgets for both isotropic and shear turbulence Toschi et al., [26]. In the present study, the mean shear $\langle \bar{S} \rangle$ is obtained by temporal averaging of the velocity field at each computational node using the exponential averaging function. The eddy viscosity in (SISM) can exhibit important properties directly from the explanation of the model itself are discussed below:

i.   When the mean shear $|\langle \bar{S} \rangle|$ is zero the original Smagorinsky model is repossess. This property render accumulative advantage for homogenous and isotropic turbulence where Smagorinsky model has already been established to function competently.

ii. In laminar flow regime $\left(|\bar{S}| = |\langle \bar{S} \rangle| \right)$ the predicted eddy viscosity faded without the stipulation of any special execution. This characteristic render a distinctive supremacy over the primary Smagorinsky model which anticipate the eddy viscosity from becoming zero in a shear regnant region in a laminar flow.

iii. In SISM the turbulent viscosity is defined as $v_T = (C_S \overline{\Delta})^2 (|\overline{S}| - |\langle\overline{S}\rangle|)$, the third property emanate due to the subtraction of mean instantaneous resolved strain rate. This dampen the degree of the eddy viscosity near the boundaries.

2. Numerical methods

The present work uses finite volume methodology (FVM) on collocated grid as proposed by Eswaran and Prakash, [27]. The detailed documentation of the method can be referred from Sharma and Eswaran, [28]. To avoid pressure velocity decoupling, Momentum Interpolation Method (MIM) originally proposed by Rhie and Chow, [29] has been used. Semi-implicit method is used for time advancement. Various upwinding schemes such ad first order upwinding (FOU), central-difference scheme (CDS) and Quadratic Upwinding Interpolation Scheme (QUICK) are deployed for convective terms. Upwinding scheme i.e. the FOU, stated above, makes the discretized sets of equations diagonally dominant thereby enhancing the convergence properties. However, FOU is extremely diffusive and is spatially a first order scheme. CDS, which is second order accurate in space, induces non-physical oscillations when applied for convective terms of the Navier-Stokes equations. The QUICK is also second order accurate in space for non-uniform grids. The convection term in equation (2) hence can be hybridized as in Equation (5) to take the advantage of convergence property of FOU and second order space accuracy of CDS.

$$CONV_{flux} = (1-\gamma)\left[CONV_{flux}\right]_{FOU} + \gamma\left[CONV_{flux}\right]_{CDS} \quad (5)$$

Where γ is the weight function have value between 0 & 1. Pure FOU is obtained for $\gamma = 0$ whereas $\gamma = 1$ results in pure CDS scheme. In present case the value of γ is chosen as 0.98 so that it is as possible to 1 to attain higher order accuracy in space. The diffusion terms are discretized spatially using CDS and temporally using Crank-Nicolson scheme. To solve the pressure Poisson, GSOR method is applied. Code parallelization is achieved using commands from the MPI library. For LES implementation SISM is used. The numerical method has been extensively evaluated various turbulent shear flows in complex geometrical configurations, [5, 29].

3. Computational details

The present problem, deals with the study of flow & heat transfer of a HSV region at the leading edge of wall mounted twisted turbine blade configuration. Figure 1 depicts the three-dimensional model of twisted turbine cascade, the geometrical details of the blade is depicted in Table I. The computations are performed at Reynolds numbers of 50000. Instantaneous flow fields, time-mean quantities are presented. The objective of the study is to elucidate the detailed physics encountered in blade passage so the grid size used to perform simulations in x, y & z

direction is $465 \times 402 \times 182$. The grid density is kept high near the walls & blade surface in order to resolve the near wall viscous effects. The H-type grid configuration is executed on the computational domain in order to capture the correct physics a small boundary layer is formed along the blade surface by using the split block tool in ICEM CFD to ensure the fine numerical resolution. The grid simulations are carried out using Nondimensional physical time step of $\Delta t = 4 \times 10^{-4}$ respectively. The minimum and maximum grid spacing range for mesh in streamwise, spanwise & pitchwise direction are given as $\Delta x = 0.0056 - 0.0070$, $\Delta y = 0.00077 - 0.0096$ and $\Delta z = 0.0034 - 0.0048$ respectively.

Table I : Cascade geometry data	
Axial chord length of the blade (C)	44
Pitch to chord ratio	1.21
Aspect ratio (Span/ Axial chord)	1.85
Maximum thickness of the blade	0.41
Minimum thickness of the blade	0.29

The boundary conditions (Nondimensional form) used in the present numerical simulation are given below:

Table II: Boundary Conditions	
Inlet	$\overline{u} = \overline{u}_{avg}, \overline{v} = 0, \overline{w} = 0, \overline{\theta} = 1 \& \frac{\partial \overline{p}}{\partial n} = 0$
Outlet	Convective outflow boundary condition proposed by Orlanski, [30] has been used. $\frac{\partial \overline{u_i}}{\partial t} + u_c \frac{\partial \overline{u_i}}{\partial n} = 0$ Here, u_c is the convective velocity at the outflow boundary plane. While the temperature $\left(\frac{\partial \overline{\theta}}{\partial n} = 0\right)$ & pressure $\left(\frac{\partial \overline{p}}{\partial n} = 0\right)$ gradient is implemented at outflow.
Top & Bottom wall	$\overline{u}_i = 0$, $\overline{\theta}_w = 0$ & $\frac{\partial \overline{p}}{\partial n} = 0$
Transverse or pitchwise	Periodic boundary condition

4. Scope and Organization of the paper

The various generic junction flow configuration has been studied so far including wall mounted wing (e.g., Devenport et al., [1]), cube (e.g., Martinuzzi et al., [3] Hussein et al., [4]) and circular cylinder (e.g., Baker, [8] Dargahi, [9] Agui et al., [10]) have increased considerably our understanding of the structure of the HSV system in front of the above-mentioned obstacles. In the

junction flow, the three-dimensional flow field is obtainable from LES results a more meticulous picture of the flow can be procured by using the eddy-resolving numerical approach. In-depth exploration of the dynamics of eddies in the HSV system and of their interactions with the other dynamically, important coherent structures in the flow is thinkable.

Our major objective:

i. Provide a perceptible characterization of the changes in the structure and dynamics of the necklace vortices.

ii. Investigate the phenomenon i.e., responsible of formation of legs of the string vortices and associated vortex surface interactions.

iii. Provide an improved understanding of the physical mechanisms that give rise to elevated levels of endwall heat transfer in junction region.

RESULT AND DISCUSSION

The flow field near the endwall region of the blade passage is dominated by the boundary layer, strong pressure gradients, and cross flow in the pitchwise direction from the pressure side to the suction side. The resulting near-wall flow field is complex and consist of strong secondary flows and vortex roll-up. When the endwall boundary layer approaches the blade row, a vortex is formed near the junction of the blade leading edge and the endwall. This vortex is termed as the leading edge horse-shoe vortex. The horse-shoe vortex splits at the leading edge, and propagates downstream into the passage on both the pressure side and the suction side of the blade passage forming two legs of the early passage vortex flows. Corner vortices are also induced in the corner formed by the blade and the hub endwall. The Figure 2 shown the various structure associated with twisted turbine blade passage.

The distribution of time-averaged streamline pattern coloured with temperature and velocity vector coloured with streamwise velocity for Re = 50000 is depicted in Figures 3 & 4. The streamline pattern and vector field reveal some distinct feature of the time-averaged horseshoe vortex (HSV) as compared to other geometrical configuration, [1-5]. The separation of the upstream boundary layer and the formation of a separation (stagnation line) on the bottom surface around the turbine blade are a consequence of the adverse pressure gradients induced by the wall mounted turbine blade. The reorganization of the boundary layer vorticity downstream of the separation line results in the formation of a system of coherent necklace vortices. The blade-endwall junction region is occupied by an approximately elliptical in shape primary horseshoe vortex (PHSV) whose sense of rotation is in the clockwise direction (positive vorticity). It should be noted that for clarity grid points have been skipped while plotting the vectors. The relative strength of the secondary flow field can be ascertained through the reference vectors plotted at the top of each figure. From Figure 3(b) it is clearly observed that four types of vortices exist in the detached region that are generated through the different

process region. This flow model can reasonably explain the flow field in the separated region on the x-y plane. Such a flow occurs at the leading edges of the turbomachinery blades. A substantial recirculation behind the blade namely PHSV1, a small secondary eddy trapped between PHSV1 and the blade called as corner vortex (CV), this is mainly formed by the separation of the boundary layer in the upstream face of the obstacle i.e. blade leading edge (LE). The surface attached vortex (SAV1) also named as counter-rotating vortex and separation vortex (SV) which is also called as secondary vortex are also reported behind the PHSV1. The existence of four types of vortices reported by Ishii and Honami, [40] i.e., corner vortex, horseshoe vortex, counter vortex & secondary vortex is confirmed in Figure 3 for bottom endwall. The HSV with a large scale can be observed as the PHSV1 just head of the turbine blade. On the other hand, the separation vortices are formed by a roll-up of the wall shear layer. Basically, this is a manifestation of the impending reattachment and thinning of the shear layer as the boundary layer is swept laterally by the favorable pressure gradients created as a result of the flow around the leading edge of the blade. There are at least two vortices rotating in the clockwise direction and one smaller vortices rotating in the opposite direction. Meanwhile for top endwall region only two vortices are formed one is PHSV2 and another one is SAV2 both are rotating in opposite direction. The exact number of vortices was seen in Figure 3 depend upon the flows speed and thickness of the blade, the number of vortices get reduced as the flow speed is increased. As compared with top & bottom endwall as shown in Figure 3 (a) and (b), it is clearly observed from the time-averaged picture that the PHSV2 shift towards upstream of the blade i.e. the core location is (x = -0.60, y = 1.82, z = -0.178) while for the PHSV1 the core location is (x = -0.61, y = 0.042, z = 0.067), and this shift of the PHSV shown by the dotted line. The size of the SAV2 is small as compared to SAV1 their respective core located at (x = -0.649, y = 1.38, z = -0.180) & (x = -0.669, y = 0.023, z = 0.066). The streamlined plot for Figure 3 (a) & (b) suggests that the spatial variability regarding the position of the center of PHSV and SAV for the streamwise direction. The velocity vector profile is less full than for a standard two-dimensional flat plate boundary layer, indicating that the adverse pressure gradient is influencing the pattern due to the blockage of the blade. It is clearly observed from the Figure 3 & 4 that strength of PHSV1 & SAV1 is higher as compared to PHSV2 & SAV2 this is because at the bottom endwall region the blade thickness is maximum as compare to top endwall region. At upstream of end wall, the location of saddle point at bottom surface is (x = -0.74, y = 0.0069, z = 0.0097) while for top surface is (x = -0.71, y = 1.85, z = 0.136), the vectors takes on the appearance of a two-dimensional boundary layer, through vortex stretching is present. Following the flow field from the saddle point toward the leading edge of the blade, the velocity vector indicates that flow in the boundary layer and outside of the boundary layer pitched downward rotated 180 deg and proved toward the saddle point, loss-free fluid outside the boundary layer stagnated at the end wall blade junction. This velocity vector field which is roughly elliptical structure, as shown in Figure 4 (a) - (b), generates an excessive backflow

by reversing fluid impinging on the end wall & leading edge of the blade. The backflow reaches maximum mean velocity and then decelerates giving the appearance of reseparation for bottom endwall between x = -0.81 and -0.51 in the vicinity of the line of low shear. In region x = -0.65 at the bottom endwall the two inflection point exist this is because the surface attached vortices (SAV1) are developed at the wall. However, the number of structures and their complexity varies with increasing Reynolds number, [6-7]. The vorticity (Ω_z) contours in the x-y plane for both top & bottom endwall are calculated using central differencing scheme, it is evident from the Figure 5 (a) – (b), the primary horseshoe vortex (Light red colour) shown by dotted arrow interact with endwall and generating opposite sign vorticity (Blue colour) via a local vortex induced pressure-gradient effect, [7] that manifest itself as a region both directly beneath the vortex and as growing tongue just trailing the vortex. Here, this negative and positive vorticity indicate the continuation of the horseshoe vortex system convecting downstream along the shear layer. This eruptive tongue in present case of high Reynolds number, i.e., increases in strength and penetration into the boundary layer and it occupies sizeable upstream distance. The primary HSV also undergo stretching. It is known that during stretching the circulation of a primary vortex will be conserved in the absence of flux or diffusion of vorticity across an endwall boundary that initially encompasses all the vortex vorticity. There are, two ways that viscosity could affect come into play. First, vorticity can diffuse across the boundary and second, the vorticity comprising the vortex could cross diffuse with the corresponding opposite sign vorticity that is generated at the surface and circulates the vortex.

The streamlines slightly above the bottom endwall in Figure 6 show some distinct features of the endwall boundary layer flow. These features are identified by the separation lines in the Figure 6. The streamlines along the blade leading edge bifurcate as they approach the saddle point. The saddle point is the location on the endwall where the zero degree incidence line meets the separation line and corresponds to the lowest friction velocity. The incoming endwall boundary layer detaches along the separation line, and secondary vortical flows are formed in the regions immediately downstream and adjacent to the separation line. This is indicated by the high concentration of the streamlines adjacent to the separation line. The strong reverse flow in the vortex regions counter the boundary layer streamlines causing them to be concentrated more densely near the separation line. The leading edge horse-shoe vortex immediately downstream of the saddle point is clearly evident in Figure 6 (a) & (c). The region between the separation line and the blade suction side in Figure 6 (a) & (c) represents the suction-side leg of the horse shoe vortex. The region along the separation line directed from the pressure side to the suction side represents the pressure-side leg of the horse-shoe vortex, and is driven by the passage pressure gradients. The suction side leg vortex and pressure side leg vortex meet together in the mid-passage region where the two separation lines in the passage merge. This location occurs close to the suction

surface, and the merger of the two vortices forms a stronger vortex known as the passage vortex. The passage vortex then travels along the blade suction surface toward the passage exit. Downstream of the pressure side separation line, the endwall boundary layer region is very thin and skewed toward the suction side. This is evidenced by the streamline concentration being sparse in this region as they turn from the pressure side to the suction side. The strong vortical motions of the pressure side leg vortex entrain most of the fluid from the incoming boundary layer and a new boundary layer forms downstream. Comparing the streamlines in Figure 6 (a) & (c) with those in the mid-span regions in Figure 6 (b) , it is clear that the turning of the streamlines inside the blade passage and around the leading edge is much greater near the endwall region which causes the cross flow here to be stronger. The uniform pressure distribution along the pressure surface span and very weak interaction of the boundary layers between the pressure surface and endwall are responsible for such flow behavior. However, the laminar boundary layer near the pressure surface leading edge may diffuse with a rise in surface pressure when the incoming flow is at high speed.

The spanwise vorticity pattern on the suction surface & pressure surface shown in Figure 7 reveals some interesting features of the boundary layer behavior. The separation lines divide the flow on the suction surface into three regimes: (i) two dimensional laminar boundary layer regime, (ii) turbulent boundary layer regime, and (iii) three dimensional flow regime.

(i). Two dimensional laminar regime: This regime extends from the leading edge to the lowest suction pressure on the suction surface and between the S2s separation lines near the two endwalls in Figure 7. The laminar boundary layer starting at the leading edge undergoes a high acceleration on the suction surface. According to Hodson and Dominy, the over-acceleration in the boundary layer causes a two dimensional separation bubble near the blend point of the circular leading edge and the suction surface. Following the re-attachment behind the separation bubble, the laminar boundary layer accelerates along the suction surface and continues to grow until the separation line S3s.

(ii). Turbulent regime: This regime is limited by the re-attachment line following the separation at S3s and trailing edge and between the S2s lines. The laminar boundary layer separates at the lowest suction pressure located at axial distance at S3s because of the adverse pressure gradient and forms another closed separation bubble. The boundary layer undergoes transition and becomes turbulent as the Reynolds number is increased it is clearly evident in Figure 7. The turbulent boundary layer grows along the suction surface and may separate again due to the adverse pressure gradient near the trailing edge to form the trailing edge wake.

(iii). Three dimensional flow regime: This regime is indicated by the region between the separation line S2s and endwall. The regime begins at the location where the suction side leg of the leading edge horse-shoe vortex and pressure side leg vortex from the adjacent blade meet on the suction surface. The pair then emerges as the passage vortex which then moves toward the span as it follows the suction surface toward the passage

exit. The distinct appearance of the separation line S2s indicates that the suction side leg vortex maintains its existence in the axial development of the passage vortex. The locations of the separation bubbles and separation lines on the blade surface are strongly influenced by the inlet flow angle and Reynolds number of the incoming flow.

Figure 8(a) – (b), is a time-averaged realization of Nusselt number distribution on the endwall. The impinging behaviour of turbulent boundary layer immediately upstream of the endwall separation point (x = -0.51) just prior to the leading edge of the blade created the streak spacing behaviour. The Figure 8 reveals that the most spatially extensive or primary region of high heat transfer is a band (red colour) located just upstream of the LE. The simulation result revealed that primary band of high heat transfer is caused by outer region boundary layer fluid that impinges on the LE of the blade and then flows down the face of the blade & hit on the endwall Praisner et al. [33, 34]. The strength of this primary band around the blade LE depends upon the Reynolds number at low Re case (not shown), the region occupied by primary band is less as compare to the high Re. The primary band of high heat transfer was found to be temporary unstable demonstrating little change. From Nusselt number plot another thin leg of high heat transfer region is observed which also wraps around the primary band and this second region is referred as secondary band. However this secondary band or region of high heat transfer was found to be much more transient in its development and behaviour. Figure 3 illustrates the time-averaged flow field data (streamlines coloured by temperature) with the corresponding time-averaged heat transfer distribution. It is clearly evident from Figure 3 that the PHSV1 is coloured by moderate concentration of temperature and this PHSV1 is rest above a region of relative low heat transfer, the SAV1 separating the two bands of high heat transfer also a region of high heat transfer upstream of SAV1 is in fact spatially coincident with SV. The vortical structures of HSV system i.e. PHSV1, SAV1, SV & DV are labeled in Figure 3. From streamline pattern it is observed that incoming hot stream of fluid striking on the leading edge of the blade and then the streamlined fluid take U-turn and this reverse flow fluid strikes on endwall region, the HSV & SV vortices rest on this reverse flow fluid while this fluid is passing over the SAV1 after that it is merging with the flow. This reverse flow fluid it separate while passing over the SAV1 and then reattaches before SV. The flow reattachment at this location may be the reason for heat transfer on endwall. As expected the strong recirculation regions formed by SAV1 results in poor heat transfer and are obvious from the contour of Nusselt number as shown in Figure 8. In case of low Re, the large recirculation (not shown), near the endwall degrade heat transfer by obstructing the fluid from the core region to replace the near endwall hot fluid.

CONCLUSION

We have carried out numerical simulations of the turbulent flow past the straight turbine blade configuration using LES approach based on (SISM) model. The alikeness between the time-averaged vorticity measurements at the junction region for different geometries (Devenport & Simpson, [1] J. Paik et al, [31] C.

Escauriaza and F. Sotiropoulos, [32]) showed that present LES (SISM) model captures utmost analogous experimental & numerical trends with good characteristic & with significant accuracy. The HSV structures particularly for bottom & top endwall are of comparable sizes. Even at bottom wall the number of vortices formed are more because of more thickness of blade. The vortices are more organized and are shed in a nearly periodic manner. The structures near the wall breakdown as a consequence of complex nonlinear interactions due to flow inertia.

REFRENCES

1. Devenport, W.J., and Simpson, R.L., 1990, "Time-dependent and time-averaged turbulence structure near the nose of a wing-body junction," J. Fluid Mech. **210**, 23.

2. Chrisohoides, A., Sotiropoulos, F., and Sturm, T.W., 2003, "Coherent structures in flat-bed abutment flow: computational fluid dynamics simulations and experiments," J. Hydraul. Eng. **129**, 177.

3. Martinuzzi. R., and Tropea, C., 1993, "The flow around surface-mounted, prismatic obstacles placed in a fully developed channel flow," J. Fluids Eng. **115**, 85 (1993).

4. Hussein, H., and Martinuzzi, R.J., 1996, "Energy balance for turbulent flow around a surface mounted cube placed in a channel," Phys. Fluids **8**, 764.

5. Paik J., and Sotiropoulos, F., 2005, "Coherent structure dynamics upstream of a long rectangular block at the side of a large aspect ratio channel," Phys. Fluids **17**, 115104.

6. Simpson R.L., 2001, "Junction flows," Annu. Rev. Fluid Mech. **33**, 415.

7. Doligalski T.L., Smith C.R., and Walker, J.D.A., 1994, "Vortex interactions with walls," Annu. Rev. Fluid Mech. **26**, 573.

8. Baker, C.J., 1980, "The turbulent horseshoe vortex," J.Wind. Eng. Ind. Aerodyn. **6**, 9.

9. Dargahi, B., 1989, "The turbulent flow field around a circular cylinder," Exp. Fluids **8**, 1.

10. Agui J.H., and Andreopoulos, J., 1992,"Experimental investigation of a three dimensional boundary layer flow in the vicinity of an upright wall mounted cylinder," J. Fluids Eng. **114**, 566.

11. Seal, C.V., Smith C.R., and Rockwell, D., 1997, "Dynamics of the vorticity distribution in endwall junctions," AIAA J. **35**, 1041.

12. Seal, C.V., and Smith, C.R., 1999, "Visualization of a mechanism for three-dimensional interaction and near wall eruption," J. Fluid Mech. **394**, 193.

13. Chen, C. H., 1995, "Assessment of a Reynolds stress closure model for appendage-hull junction flows," J. Fluids Eng. **117**, 557.

14. Fu, S., Rung, T., Thiele, F., and Zhai, Z., 1997, in Proceedings of the 11th Symposium on Turbulent Shear Flows, edited by M. Lesieur, B. E. Launder, G. Binder, and J. H. Whitelaw (Grenoble, France), pp. 6.7–6.12.

15. S. Parneix, S., Durbin, P.A., and Behnia, M., 1998, "Computation of 3-D turbulent boundary layers using the V2F model," Flow, Turbul. Combust. **60**, 19.

16. Apsley, D., and M. Leschziner, M., 2001, "Investigation of advanced turbulence models for the flow in a generic wing-body junction," Flow, Turbul. Combust. **67**, 25.

17. Rodi, W., 1997, "Comparison of LES and RANS calculations of the flow around bluff bodies," J. Wind. Eng. Ind. Aerodyn. **69**, 55.

18. S.C. Krajnović´, S.C., and Davidson L., 2002, "Large-eddy simulation of the flow around a bluff body," AIAA J. **40**, 927.

19. Rodi, W., Ferziger, J., Breuer, M., and Pourquié, M., 1997, "Status of large-eddy simulation: Results of a workshop," J. Fluids Eng. **119**, 248.

20. Shah, K. B., and Ferziger, J. H., 1997, "A fluid mechanicians view of wind engineering: Large eddy simulation of flow past a cubic obstacle," J. Wind. Eng. Ind. Aerodyn. **67**, 211.

21. Saha, A.K., and Acharya, S., 2003, "Parametric study of unsteady flow and heat transfer in a pin-fin heat exchanger," International Journal of Heat and Mass Transfer. **46(20)**, 3815 (2003).

22. Murata, A., Shibata R., and Mochizuki, S., 1991,"Effect of cross-sectional aspect ratio on turbulent heat transfer in an orthogonally rotating rectangular smooth duct," International Journal of Heat and Mass Transfer. **42**, 3803.

23. Moin P., Squires K., Cabot, W., and Lee, S., 1991, "A dynamic subgrid-scale model for compressible turbulence and scalar transport," Physics of Fluids - A, **3(11)**, 2746.

24. Smagorinsky, J., 1963, "General circulation experiments with the primitive equations: I. The basic equations," Monthly Weather Review, **91(3)**, 99.

25. Lévêque, E., Toschi, F., Shao, L., and Bertoglio, J.P., 2007, "Shear-improved smagorinsky model for large-eddy simulation of wall-bounded turbulent flow," Journal of Fluid Mechanics. **570**, 491.

26. Toschi, F., Lévêque, E., and Ruiz-Chavarria, G., 2000, "Shear effects in nonhomogeneous turbulence," Physics Review Letters, **85**, 1436.

27. Eswaran, V., and Prakash S., 1998, "A finite volume method for Navier-Stokes equations," In Third Asian CFD Conference. Bangalore, India, Volume 1.

28. Sharma, A. and Eswaran V., 2003, "A finite volume method. In Muralidhar, K. & Sundararajan, T. Computational Fluid Flow and Heat Transfer," 2nd ed. Narosa Publishing House, New Delhi. Ch. 12. 445.

29. Rhie, C.M., and Chow, W.L., 1983 "Numerical study of turbulent flow past an airfoil with trailing edge separation," AIAA Journal, **21**, 1525.

30. Orlanski, I., 1976 "A simple boundary condition for unbounded flows," Journal of Computational Physics. **21**, 251.

31. Paik, J., Escauriaza, C., and Sotiropoulos, F., 2007 "On the bimodal dynamics of the turbulent horseshoe vortex system in a wing-body junction," Phys. Fluids **19**, 045107.

32. Escauriaza, C., and Sotiropoulos, F., 2011, "Reynolds Number Effects on the Coherent Dynamics of the Turbulent Horseshoe Vortex System," Flow Turbulence Combust. **86**, 231.

33. Praisner, T. J. and Smith, C. R., 2005, "The Dynamics of the Horseshoe Vortex and Associated Endwall Heat Transfer: Part I - Temporal Behavior," ASME Turbo Expo. Proceedings of GT **69088**, 899.

34. Praisner, T. J. and Smith, C. R., 2006, "The Dynamics of the Horseshoe Vortex and Associated Endwall Heat Transfer—Part II: Time-Mean Results," J. Turbomachinery **128**, 755.
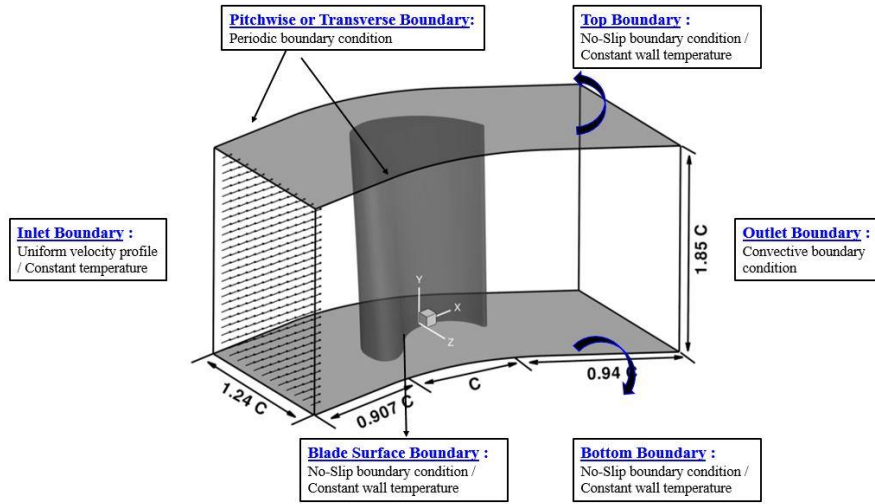
Figure 1: Three-dimensional computational domain along with the geometrical parameters governing the flow physics.
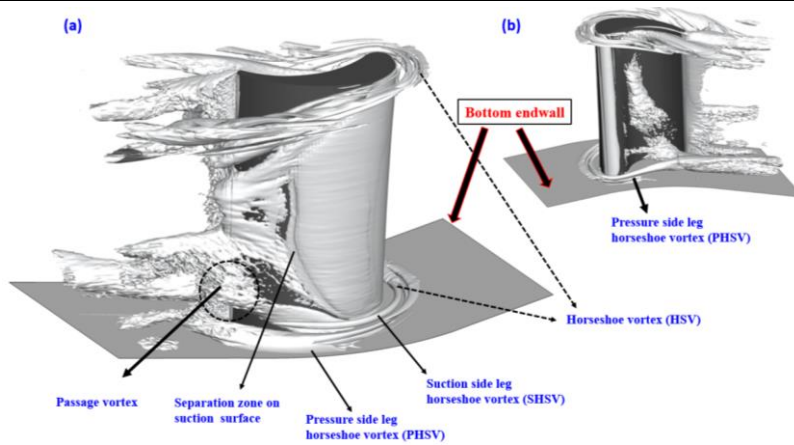

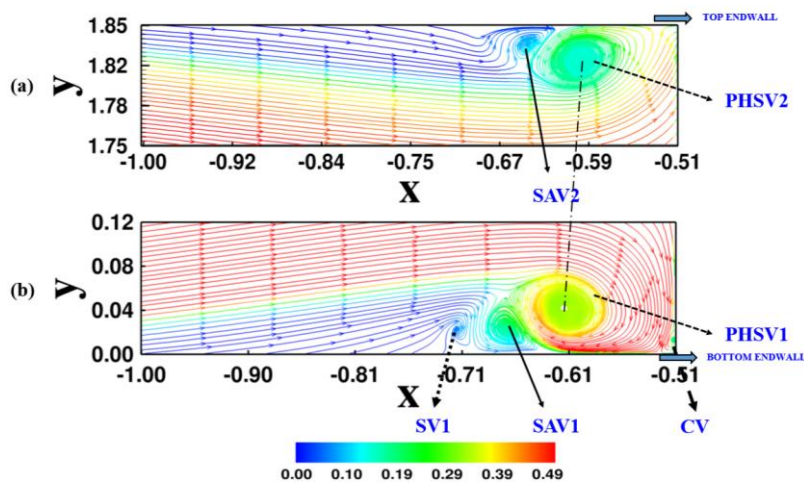Figure 2: Time –Averaged Iso-Surface of Q-criteria (Structure associated with twisted blade).

Figure 3: Time-averaged streamline pattern coloured with temperature at the blade endwall

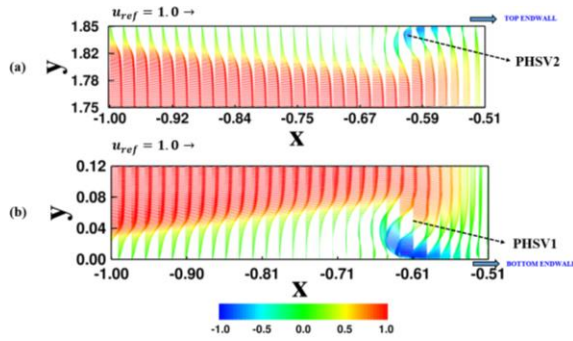junction region (a) Top endwall, (b) Bottom endwall for Re =50000.

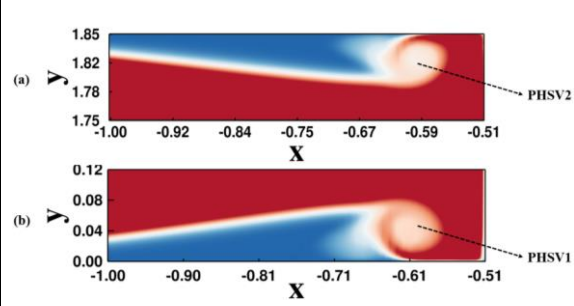| Figure 4: Time-averaged secondary velocity vectors coloured with streamline velocity at the blade endwall junction region (a) Top endwall, (b) Bottom endwall for Re =50000 | Figure 5: Vorticity (Ω_z) at Blade Endwall Junction (a) Top surface & (b) Bottom surface for Re = 50000. |

(a)   (b)   (c)

-1.00 -0.71 -0.43 -0.14 0.14 0.43 0.71 1.00
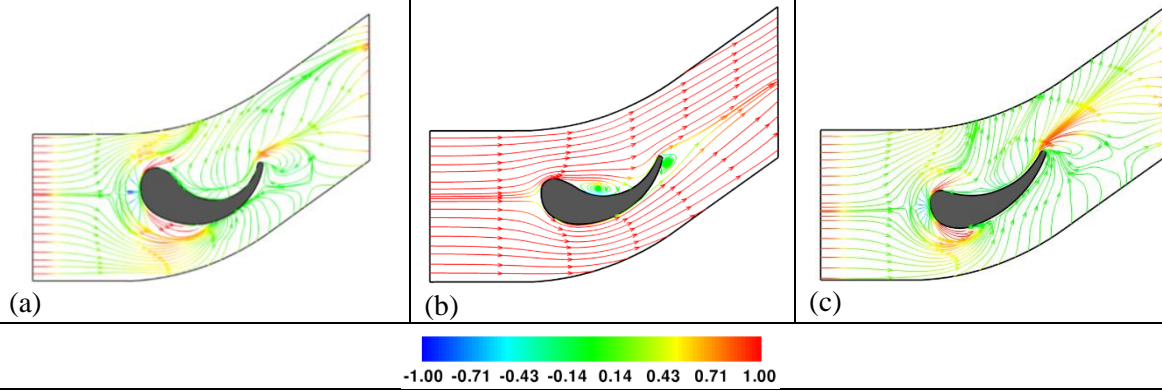
Figure 6: Variation of time–averaged spanwise streamlines pattern coloured with streamline velocity at (a) y = 0.0 (b) y = 0.92 & (c) y = 1.85 for twisted blade.
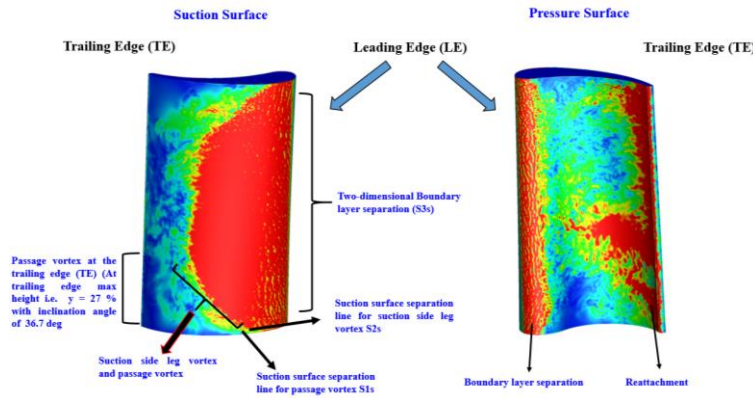

Figure 7: Variation of instantaneous spanwise vorticity for both suction & pressure surface of twisted blade.

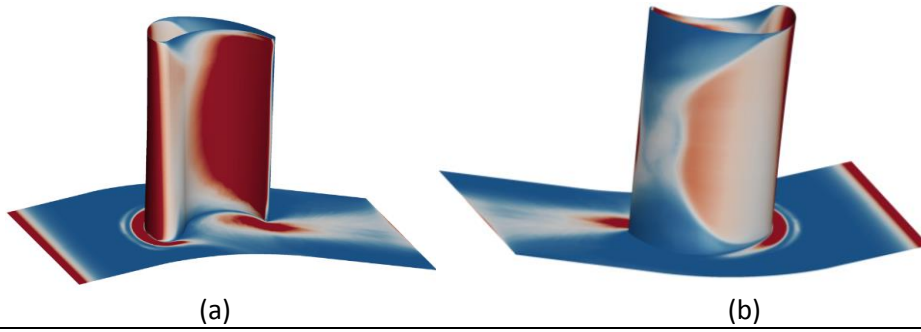10   Copyright © 2018 by NAPC

Figure 8: Time-averaged Nusselt number contours for both (a) suction side (b) pressure side for Re = 50000